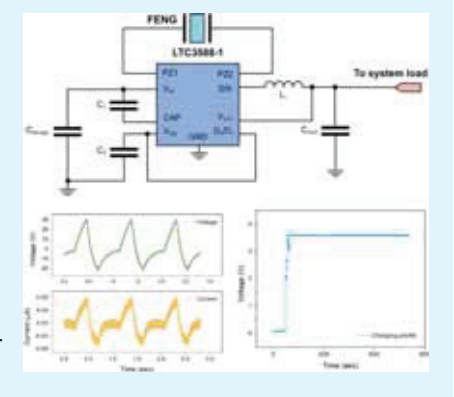


# Flexible Ferroelectret Polymer for Self-Powering Devices and Energy Storage Systems

Yunqi Cao, † José Figueroa, † Juan J. Pastrana, † Wei Li, ‡ Zhiqiang Chen, § Zhong Lin Wang, I and Nelson Sepúlveda\*, † [6]

Supporting Information

**ABSTRACT:** Applying flexible materials for energy scavenging from ambient mechanical vibrations is a clean energy solution that can help alleviate electrical power demands in portable devices and wearable electronics. This work presents fundamental studies on a flexible ferroelectret polymer with a strong piezoelectric effect and its interface with self-powered and energy storage systems. A single-layered device with a thickness of 80  $\mu$ m was used for characterizing the device's output voltage, current, transferred charge, and energy conversion efficiency. The potential capability of harvesting mechanical energy and delivering to system load is demonstrated by integrating the device into a fully integrated power management system. The theory for determining the harvested energy that is ultimately delivered to external electronic loads (or stored in a battery) is discussed. The maximum power delivery is found to be for a 600 M $\Omega$  load, which results in a device power density of 14.0 W/m<sup>3</sup> for input mechanical forces with a frequency around 2 Hz.



KEYWORDS: ferroelectret, piezoelectric, nanogenerator, flexible, energy harvesting, energy conversion, power management, self-powering

# 1. INTRODUCTION

With the incredible growth of the internet over the past few decades, the world's economic structure has been rapidly shifted to rely heavily on information technology. Not long ago, it was enough for a mobile phone to be able to make calls and send texts. Nowadays, mobile phones are essentially terminals of all kinds of information and utilities. Internet of Things and big data enable data exchange among health monitor apps, wireless sensor system, and smart automation to create a more robust and direct way to integrate real-world decision-making processes into artificial intelligence networks. Hence, multifunctionalities have been imposed to personal electronic devices such as smart phones and even bracelets. However, the future progress of all these technological advances is tied to the energy budget that comes with all these tools. Self-powering technologies<sup>1-4</sup> that convert ambient energy sources from multiple forms (e.g., solar, 5,6 thermal<sup>7,8</sup> and mechanical<sup>9-11</sup>) to electricity have become potential energy solutions for the smart, multifunctional phones and wearable electronics.

However, the path for a solution to the increasing energy demands needs to be comprehensive and inclusive. Approaches should consider scavenging, storing, and using as many different forms and magnitudes of energy. Unlike solar

energy, energy produced by random mechanical vibrations can be obtained nearly at any time from multiple sources. Energy harvesting devices such as piezoelectric (PENG), 12,13 triboelectric (TENG), 14-17 and ferroelectric (FENG) 18-20 nanogenerators that are capable of converting kinetic energy to electrical energy are considered to be the most promising devices for integrated self-powered systems.<sup>21</sup> Even though those nanogenerators exhibit a piezoelectric effect, the origins of the piezoelectricity are quite different. PENG usually use inorganic nanopiezoelectric materials such as ZnO nanoparticles and nanowires and their flexibility can be achieved by their integration with soft substrates such as polyimide (PI), polyurethane acrylate, etc. TENG make use of the triboelectric effect and are often considered at the device level for highefficiency energy harvesting. Their power densities can be as high as 313 W/m<sup>2,22</sup> Alternatively, FENG is fully based on flexible electroactive thin film polymer which utilizes the ferroelectricity of polypropylene ferroelectret (PPFE) films<sup>23,24</sup> by introducing trapped surface charges into neutral PP films. 25-29 Inside the PPFE film, engineered macroscale

Received: February 8, 2019 Accepted: April 19, 2019 Published: April 19, 2019

<sup>&</sup>lt;sup>†</sup>Department of Electrical and Computer Engineering, Michigan State University, East Lansing, Michigan 48824, United States

<sup>&</sup>lt;sup>‡</sup>Department of Electrical Engineering and Computer Sciences, University of California Berkeley, Berkeley, California 94720, United States

<sup>§</sup>School of Mechano-Electronic Engineering, Xidian University, Xi'an, Shaanxi 710071, China

School of Materials Science and Engineering, Georgia Institute of Technology, Atlanta, Georgia 30332, United States

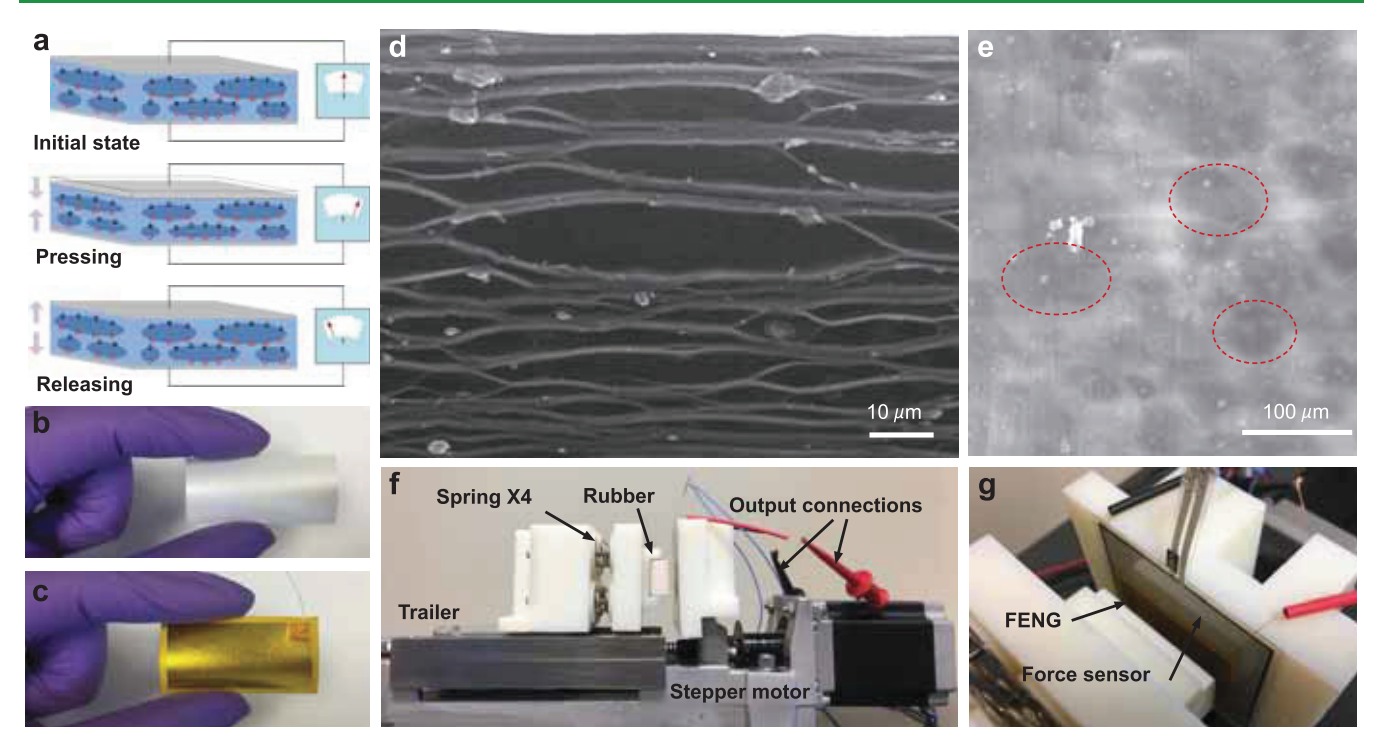


Figure 1. (a) Working principle of a ferroelectric nanogenerator. (b) Photography of a 20 mm × 40 mm PPFE film. (c) Photography of the final device with PI protective layer (20 mm × 40 mm). (d) Cross-sectional view SEM image of PPFE film with cellular structure. (e) Top-view SEM image (back-scattered electrons) of PPFE film, where darker regions are observed where voids are present. (f) Photography of the experimental setup for characterizing the electric output under various mechanical loads. (g) A close-up view of (f).

voids with opposite polarity charges trapped on top and bottom surfaces are continuously distributed, forming giant permanent dipoles. The piezoelectric coefficient  $(d_{33})$  value can be as high as 300 pC/N.<sup>30</sup> An external mechanical load would induce a relative movement of the charged surfaces with opposite polarities. The changing of dipole moment alters the electric field distribution inside the film and therefore induces free charges at the electrodes, which can be used for powering electronic devices, programming resonator frequencies,<sup>31</sup> or sensing stress level.<sup>32</sup> Although there is a significant amount of energy dissipated due to random mechanical vibrations in the environment, there are a number of challenges before reaching the ultimate goal of completely harvesting the mechanical energy from these sources. But any step toward this goal should include comprehensive studies that involve the complete energy harvesting system, from the mechanical energy input to the delivered/stored electrical energy.

The majority of the work done in nanogenerators has been focused on improving individual device performance, 33-36 which involves research on material synthesis and device characterization in terms of open circuit voltage  $(V_{oc})$  and short circuit current  $(I_{sc})$ . However, these two parameters are ideal values that do not provide relevant information for real applications. Furthermore, outputs of piezoelectric energy harvesters are also pulses with variable frequencies and irregular amplitudes, which means that their output cannot be connected directly to an energy storage unit (i.e., direct charging), since it will damage the battery or at least reduce its lifetime significantly. Thus, before nanogenerators can be connected to batteries, their output needs to be modulated to a constant voltage, constant current source, with a very small ripple tolerance. Accomplishing the integration requirements requires a deep understanding of the mechanisms that

influence amplitude and frequency in the electrical output of a nanogenerator, the energy losses in the energy harvesting process, and the required electronic configurations. Furthermore, nanogenerators typically suffer from very low currents (although their voltage outputs are very large) and a large impedance mismatch with the load (or energy storage unit). Therefore, the power modulation circuit between the nanogenerator and the energy storage unit needs to step down the voltage, provide a matching impedance that maximizes efficiency, and be characterized for amplitude and frequency variations in the mechanical input. This research presents a study that addresses all these factors.

In this work, we design, demonstrate, and validate a complete system, from nanogenerator device to rechargeable battery, for harvesting ambient kinetic energy. In the process, we fully describe the corresponding, applicable theory for characterizing the generated and stored power as well as the system's energy efficiency. The device physics is briefly explained, followed by a study where the effects of the force amplitude and frequency variations in the mechanical input on the generated output are described. Characterization experiments are carried out in terms of open circuit voltage  $(V_{oc})$ , short circuit current  $(I_{sc})$ , and output charges  $(Q_{sc})$  on a 20 mm × 40 mm single-layer device. The maximum power is measured under different loads with various input mechanical forces, and the maximum surface energy density is determined. This study allows for an understanding of the optimal conditions for which the energy transfer is more efficient, and a power modulation circuit is designed accordingly. Energy efficiency was defined as the ratio of the average electrical output energy to the average mechanical energy. The designed power management circuit is found to be especially useful for energy harvesting devices with ultrahigh impedance;

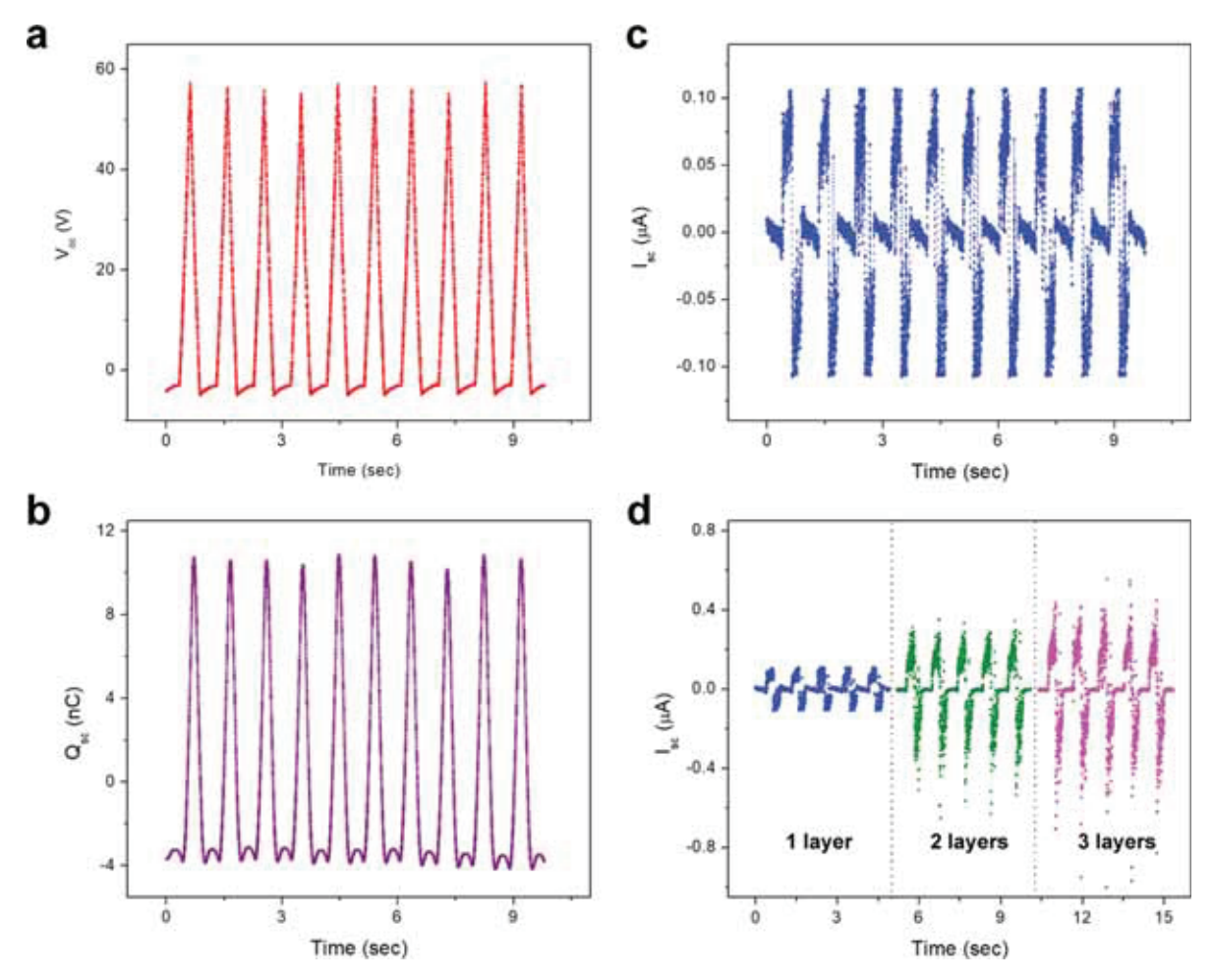


Figure 2. Electrical output for single-layer device. (a) Experimental measurement of an open circuit voltage  $(V_{oc})$ . (b) Transferred charge output  $(Q_{sc})$ . (c) Experimental measurement of the short circuit current  $(I_{sc})$ . (d)  $I_{sc}$  for multiple-layered devices.

which is a major current bottleneck in nanogenerator technologies. With either periodic or random mechanical force input, the circuit can deliver a regulated direct current (DC) power. Finally, the complete system is characterized and integrated in multiple real applications; which include charging a lithium battery and powering an liquid-crystal display (LCD) screen, thermometer, and humidity sensor.

### 2. RESULTS AND DISCUSSION

2.1. Characterization of Electric Output. The device used in this work is a thin film flexible multilayer structural device with a 80  $\mu$ m PPFE film sandwiched in between two 500 nm thin film metal electrodes (Figure S3, Supporting Information). The device is then encapsulated in between two 20  $\mu$ m thick PI protective layers. The PPFE film is the active material of the device that contributes to the conversion of mechanical energy to electrical energy, and it consists of continuously distributed ellipsoid air voids, each with two oppositely charged surfaces (see Figure 1a). Each giant engineered void forms a permanent macroscale dipole moment and constitutes a polarization field across the PPFE film thickness. When an external mechanical load is applied that generates compression of the film along the thickness direction, the size of the dipoles changes, generating a change in the polarization field and a time-varying electric field. This time-varying electric field (and the generated displacement current) can be applied to an external load by the metal

electrodes on each surface of the film. Further details on the fabrication of the device can be found in the Supporting Information. Given the capacitive nature of the material, the accumulated free charges generate an open circuit voltage  $(V_{\rm oc})$  across the film and can be expressed as

$$V_{\rm oc}(t) = \frac{Q(t)g(t)}{\epsilon A} \tag{1}$$

where Q is the accumulated charge at electrodes, g is the thickness of the PPFE film,  $\epsilon$  is the dielectric constant of PPFE, and A is the contact area of the device. This  $V_{\rm oc}(t)$  is the generated electric field to compensate for the change in the polarization field during mechanical pressing. The direct proportionality between  $V_{\rm oc}(t)$  and Q(t) indicates that both quantities follow the same dynamic behavior and are in phase, since g(t) and Q(t) are both synchronized with the applied force. Generated charges (i.e., Q(t)) can be collected and sent to external circuits or loads. When the external load is a short circuit, the short circuit current  $(I_{\rm sc})$  is given by

$$I_{\rm sc}(t) = \frac{\mathrm{d}Q(t)}{\mathrm{d}g} U_{\rm in} \tag{2}$$

where  $U_{\rm in}$  is the compression velocity due to a mechanical input. It is shown in eqs 1 and 2 that although the fundamental operation mechanism is different from piezoelectric materials (piezoelectricity is at the atomic scale, whereas PPFE films are

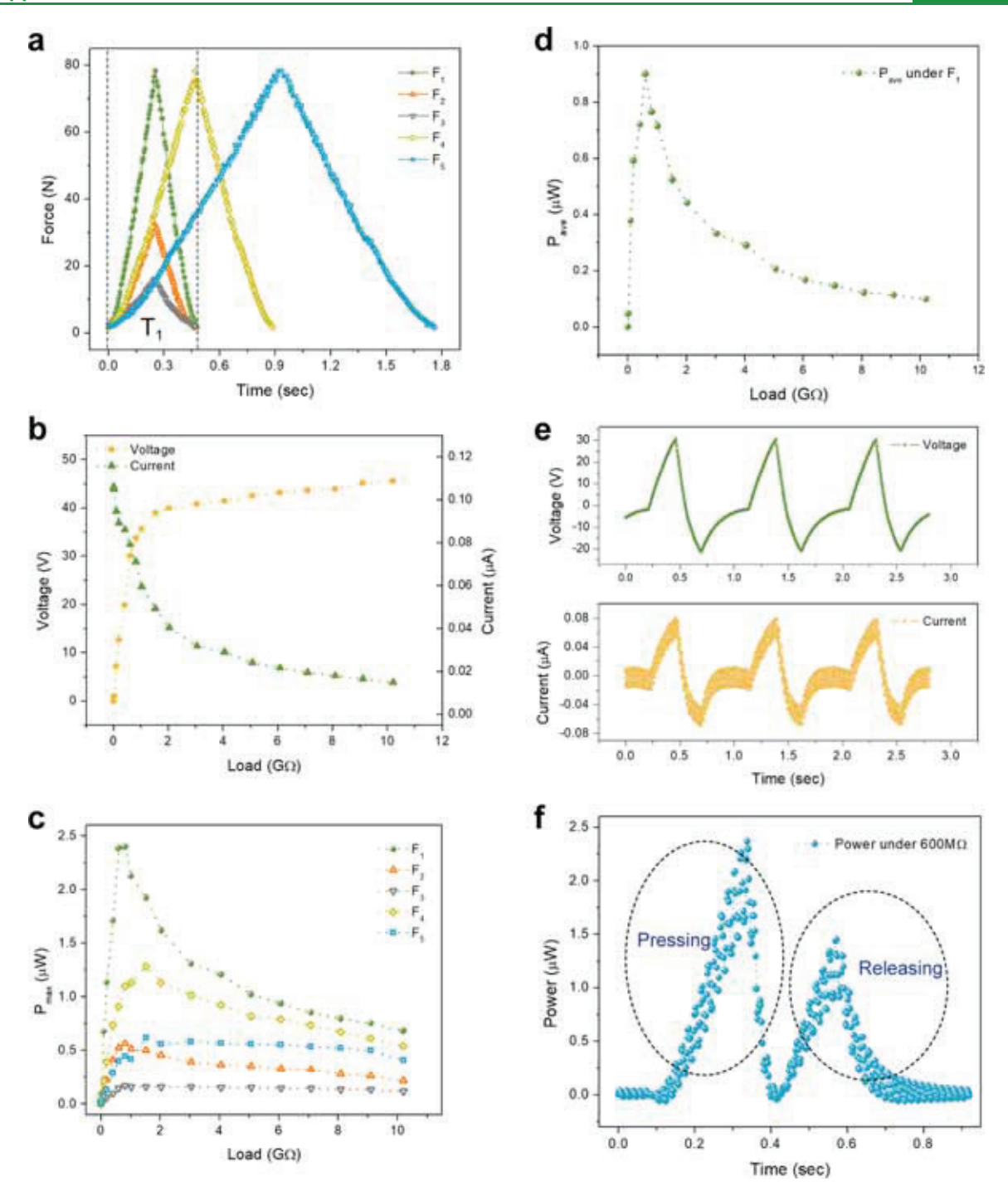


Figure 3. Electrical response of a single-layer device for different mechanical inputs. (a) Forces with different amplitudes and velocities used for the electromechanical characterization. (b) Voltage and current output with various resistive loads under  $F_1$ . (c) The maximum instantaneous power with various loads under different force inputs described in (a). (d) Average power delivery from a single press and release cycle with various loads. (e) Output voltage and current under  $F_1$  with a 600 MΩ load. (f) Output power under  $F_1$  with a 600 MΩ load.

based on macroscale dipoles), it still exhibits a piezoelectric electromechanical response, i.e., it generates a voltage signal of increasing magnitude upon compressive mechanical load until maximum compression is achieved; followed by a voltage signal of decreasing magnitude when released. Further details in the piezoelectric effect and its relation to the device are found in the Supporting Information. Figure 1b,c shows photographs of a 20 mm  $\times$  40 mm PPFE film and a single-layer device of the same size with protective polyimide (PI) coatings and connection wires, respectively. Figure 1d,e

provides scanning electron microscopy (SEM) images of PPFE films. Since the inorganic silica stress concentrators (particles in Figure 1d) are randomly distributed, ellipsoid shape voids with very different sizes are created upon the bidirectional stretching process (see detailed fabrication process in the Supporting Information). The top SEM image shown in Figure 1e shows darker regions where ellipsoids are present.

The following describes the experiments that were completed to characterize the electrical signals and maximum

power output generated by a single-layer device due to a mechanical input. As shown in Figure 1f, a stepper motor is used as a linear actuator, which pushes a rubber piston toward a single-layer device (surface area of 20 mm × 40 mm) mounted on the back scaffold. A trailer is used to transfer the rotation of the motor to a linear displacement of the piston, and the linear mechanical load is realized by using four mechanical springs connected in parallel. The applied force amplitude and its velocity is computer-controlled by programming the duty cycle and number of pulses applied to the stepper motor. A force sensor (A502, Tekscan, Inc) is placed behind the device to monitor the real time force applied to the device (Figure 1g shows a close-up view for clarity).

For the single-layer device used in this experiment, a linear external mechanical load is applied periodically to the device, where each cycle contains a pressing stage, followed by a releasing stage with a symmetric profile. The electrical outputs in terms of  $V_{oc}$ ,  $I_{sc}$ , and transferred charges  $Q_{sc}$ , which in the ideal case would be equal to the accumulated charge at the electrodes,<sup>37</sup> are measured and presented in Figure 2. Figure 2a shows  $V_{oc}$  for a periodic force with the profile shown in Figure 3a corresponding to  $F_1$ . For this cyclic load with a peak force of 78 N and frequency of 2 Hz (period of 0.5 s), a single-layer device outputs a maximum  $V_{\rm oc}$  of around 56 V, given that the root mean square voltage  $V_{\rm RMS}$  can be expressed as  $V_{\rm RMS}^2 = \frac{1}{T} \int_0^T V_{\rm oc}^2(t) dt$ , thus  $V_{\rm RMS}$  is calculated to be 29 V. It should be noted how the  $V_{\rm oc}$  profile follows an increasing/ decreasing profile that follows the compression/release profile of the applied force  $(F_1)$ . This is the expected behavior for linear coupling between mechanical domain and electrical domain of the piezoelectric material but is different from the one observed in for the same type of device or in other reports of nanogenerators that operate under similar phenomena based on the displacement current. The rationale for these differences lies on the mismatch of the internal impedance of FENG and the voltmeter for  $V_{\rm oc}$  measurement. When  $V_{\rm oc}$  is being measured, there should be no current flowing through the device-voltmeter circuit loop.  $V_{\rm oc}$  should be proportional to the strain (relative change in the film thickness), which is also linearly related to the applied mechanical stress. Therefore, profiles for  $V_{\rm oc}$  (see Figure 2a) and force  $F_1$  (Figure 3a) follow a similar pattern. However, unlike  $V_{\rm oc}$ ,  $I_{\rm sc}$  is originated from the displacement current, which is proportional to the derivative of the polarization charge (or accumulated charge  $Q_{so}$  in this case). Therefore,  $I_{sc}$  shows a bipolar square wave profile as the derivative form of a triangular wave (Figure S5, Supporting Information). When a voltmeter with much lower internal resistance R (note that the capacitance of FENG is ~17-30 pF/cm<sup>238</sup>) is connected for obtaining  $V_{oc}$ , the measured voltage V is determined by V = IR; where I is the nonzero current flowing through the devicevoltmeter loop. During each pressing and releasing time period T, the transferred charge can be determined by taking the integral of  $I_{sc}$  as  $Q(t) = \int_0^T |I_{sc}(t)| dt$ , which is equal to 11.5 nC (see Figure 2b), which also follows the same profile as  $V_{oc}$  and eq 1. However,  $I_{sc}$  comes from the change in that charge (Q(t)) per unit change in thickness (g(t)) and therefore presents a bipolar profile for every  $V_{\rm oc}$  cycle. Instruments with relatively low internal resistance will dissipate the generated displacement current in their internal resistance and display a voltage profile that follows the product of the displacement current and the internal resistance. The profiles for  $V_{oc}(t)$  and

the applied force  $F_1$  become closer to each other and more synchronized in time as this internal resistance increases.<sup>39</sup> In this case, the device supplies a peak current  $I_{sc}$  of 0.1  $\mu$ A, which corresponds to a root mean square current  $I_{RMS}$  of 73 nA. Here, the same method of determining  $V_{\rm RMS}$  is used for calculating  $I_{\rm RMS}$  by substituting  $V_{\rm oc}$  with  $I_{\rm sc}$  (see Figure 2c), with a cyclic profile that crosses  $I_{sc} = 0$  nA at the time of peak voltage in  $V_{oc}(t)$ . To increase the output current, the simplest way is to increase the capacitance of the device by increasing the area. This can be easily achieved by folding a larger device multiple times into a smaller size or by stacking the several single-layer devices into a multilayer structure. Figure 2d shows the relation between  $I_{sc}$  output and stacking layers (see Figure S8 in the Supporting Information for  $V_{oc}$  and  $Q_{sc}$  of multilayer structure); where an increasing current peak is found to be proportional to the number of layers. The functionality of multiple-layer devices is found in the Supporting Information,

To obtain an optimal power delivery, it is necessary to look at both electric output parameters: voltage and current, produced by mechanical forces with different profiles. For this characterization, linear forces with different amplitudes and velocities are introduced (see Figure 3a), and the electromechanical responses due to various resistive loads are measured.  $F_1$ ,  $F_2$ , and  $F_3$  have the same pressing and releasing cycle but different force amplitudes:  $A_1 > A_2 > A_3$ ; where  $A_i$  is the force amplitude of force  $F_i$ . On the other hand,  $F_4$  and  $F_5$ have the same force amplitude as  $F_1$  but longer cycles:  $T_5 > T_4$ >  $T_1$ , where  $T_i$  is the duration of a single pressing/releasing cycle of force  $F_i$ . Since  $V_{oc}(t)$  is proportional to the compression distance and  $I_{sc}(t)$  is proportional to the compression velocity, the force with greater amplitude and shorter pressing/releasing cycle should deliver higher voltage and current output, therefore higher power to the external loads. This would correspond to  $F_1$  from the applied forces (see Figure 3a). Figure 3b shows the voltage and current output under  $F_1$ , for a wide range of load resistances. The instantaneous peak power delivered to the load is also measured for all forces and plotted as a function of load resistance, as shown in Figure 3c. Table 1 summarizes the

Table 1. Power Delivery under Different Loads

| force: $F_i$                           | $F_1$ | $F_2$ | $F_3$ | $F_4$ | $F_5$ |
|--|-------|-------|-------|-------|-------|
| amplitude: $A_i$ (N)                   | 78    | 33    | 16    | 78    | 78    |
| cycle: $T_i$ (s)                       | 0.47  | 0.47  | 0.47  | 0.89  | 1.76  |
| peak power: $P_{\rm max}~(\mu { m W})$ | 2.38  | 0.56  | 0.17  | 1.28  | 0.61  |

amplitude and cycle of each force with related output instantaneous peak power. The maximum power delivery is found to be at around 600 M $\Omega$ . It is noted that the power output is more sensitive to force amplitude than to speed or frequency. Doubling the force amplitude produces a 4X increase in power output, whereas decreasing the cycle by a half produces a 2X increase in that same parameter. This measurement is in agreement with theory, since increasing the force amplitude has an effect on  $V_{\rm oc}(t)$  (force amplitude is directly proportional to g(t)) and and  $I_{\rm sc}(t)$  (force amplitude is directly proportional to the generated displacement current), whereas the compression/releasing velocity only affects  $I_{\rm sc}(t)$  (see eqs 1 and 2). Therefore, the device is more suitable for harvesting energy from environments involving large, slow motion mechanical energy sources, such as human footstep, <sup>40</sup>

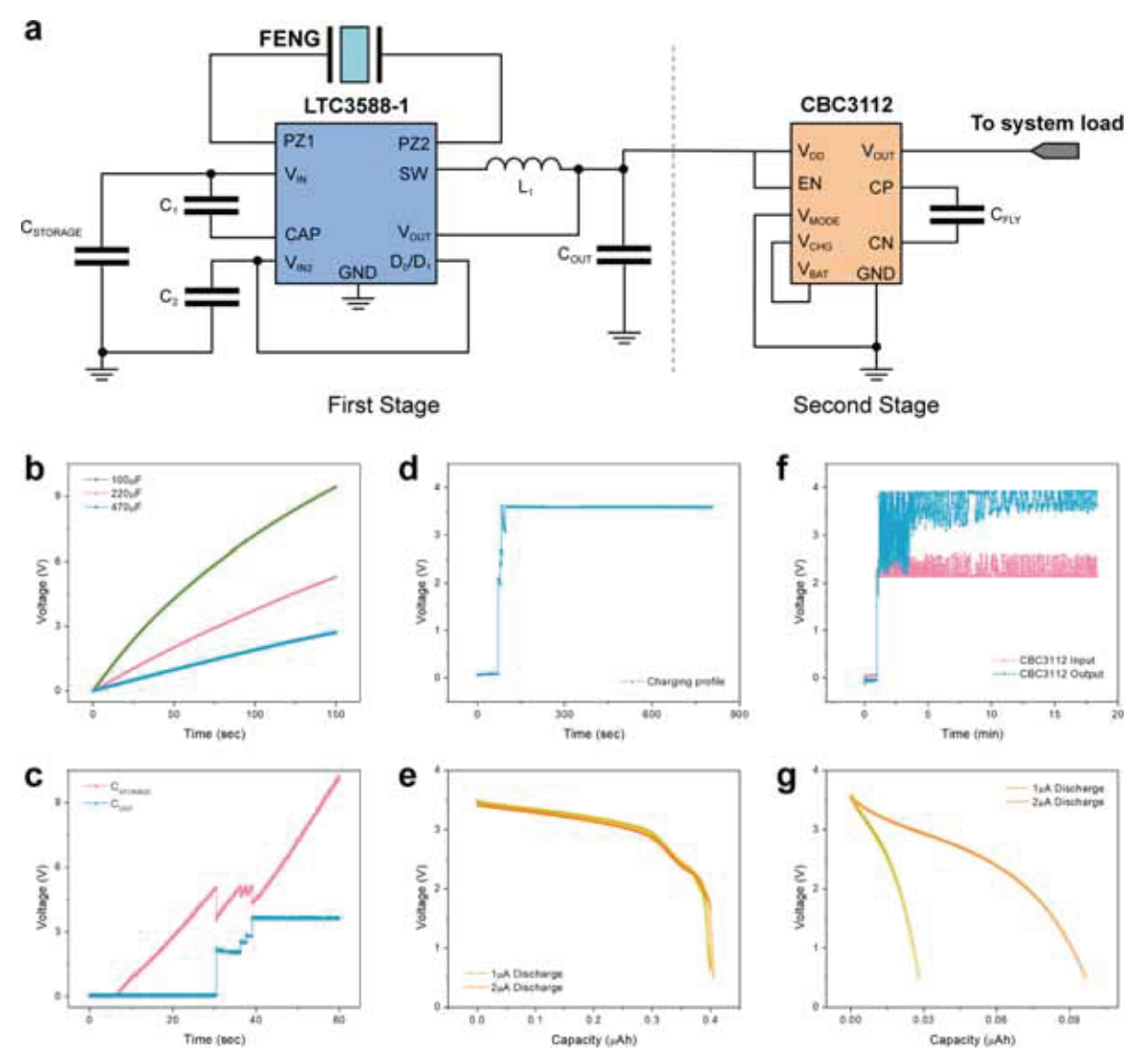


Figure 4. Energy harvesting module. (a) A comprehensive energy harvesting system,  $C_1 = 1 \mu F$ ,  $C_2 = 4.7 \mu F$ ,  $C_{OUT} = 47 \mu F$ ,  $L_1 = 22 \mu H$ , and  $C_{FLY} = 0.1 \mu F$ . (b) Direct charge of capacitors with different capacitances. (c) Voltage regulation of the nanopower energy harvesting power supply LTC3588-1. (d) Charging profile of rechargeable solid state battery CBC012. (e) Discharging profile of rechargeable solid state battery CBC012. (f) Voltage regulation of integrated power management chip CBC3112. (g) Discharging profile of integrated energy storage unit in CBC3112.

ocean waves, <sup>41</sup> wind blow, <sup>42,43</sup> etc. Figure 3d shows the average power output delivered by each pressing and releasing cycle with various loads. The maximum average power  $P_{\rm ave} = \frac{1}{T} \int_0^T I(t) \times V(t) {\rm d}t$  is estimated to be around 0.902  $\mu{\rm W}$  with a 600 M $\Omega$  load, with a device power density ( $P_{\rm v}$ ) of ~14.09 W/m³, for input force  $F_{\rm l}$ , which has a frequency of 2.13 Hz. The voltage and current output for this load are also plotted in Figure 3e and the instantaneous power as a function of time during a single cycle is shown in Figure 3f.

**2.2. Energy Conversion Efficiency.** For energy harvesting applications, it is important to evaluate the energy conversion efficiency  $(\eta)$  from mechanical energy to electrical energy. This is often defined by the total electric energy output  $(W_{\rm E})$  divided by the total mechanical energy input  $(W_{\rm M})$  per cycle. Since the spring softening effect is limited and the electromechanical coupling can be simply described by a spring model (see Supporting Information), the mechanical energy input can also be expressed by the elastic potential energy as below

$$W_{\rm M} = \frac{1}{2} k \Delta g^2 \tag{3}$$

where k is the spring constant of PPFE film and  $\Delta g$  is the maximum change in thickness upon compression.  $W_{\rm E}$  can be determined as the power delivered to the load as

$$W_{\rm E} = \int V \times I \, \, \mathrm{d}t \tag{4}$$

where V and I are voltage and current across the load. By using Young's modulus of PPFE as  $Y=1\times 10^6~{\rm N/m^2},^{44}$  the spring constant of the device used in this experiment becomes  $k={\rm YA/g}=10^7~{\rm N/m}$ . For calculating the operation efficiency in this system, it is necessary to linearize the system around the operating point first and then determine the ratio of the electrical energy produced by the system to the mechanical energy delivered to the system. For the present system, the maximum conversion efficiency  $\eta_{\rm max}$  is determined to be around 0.14% for  $F_1$  with a load of 600 M $\Omega$  (details on the linearization around the operation point and calculation of the energy efficiency are found in the Supporting Information).

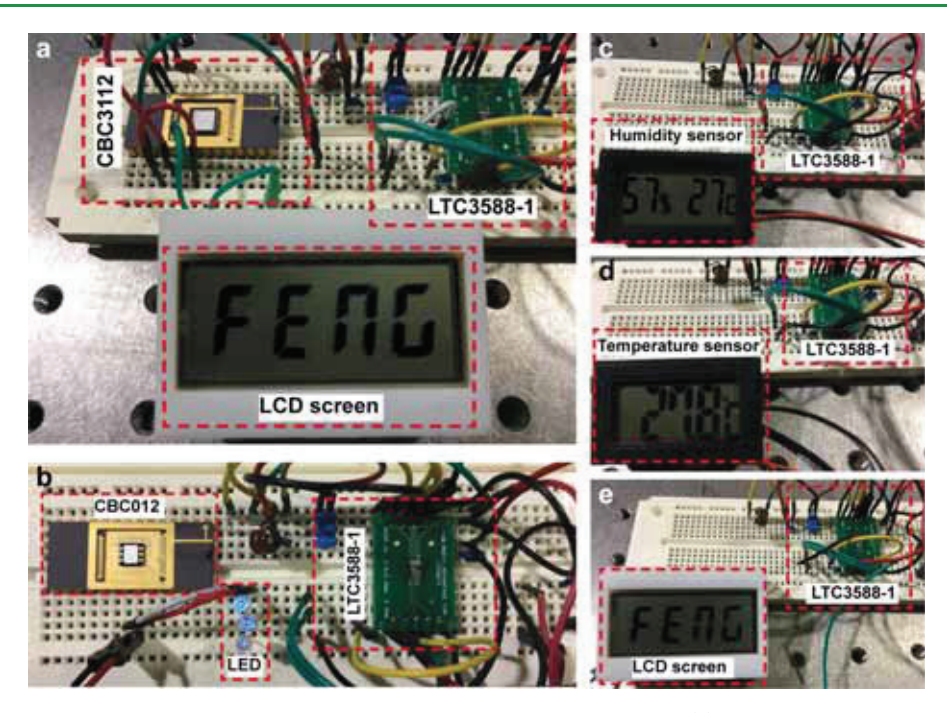


Figure 5. Energy harvesting demonstration of powering electronic devices and charging battery. (a) Powering LCD screen by combing a two-stage energy harvesting system. (b) Charging the rechargeable solid state battery CBC012, the stored energy is used for powering three blue LED lights. (c) Powering humidity sensor by a one-stage energy harvesting system. (d) Powering temperature sensor by a one-stage energy harvesting system. (e) Powering LCD screen by a one-stage energy harvesting system.

2.3. Integrated Energy Harvesting System. The simplest energy harvesting system can be achieved by direct charging<sup>45</sup> through a bridge rectifying diode circuit. However, the unregulated voltage output has been proven to deliver very low efficiencies and will significantly reduce the life-span of a rechargeable battery or electric device which often requires a constant DC input. To effectively harvest the energy from ambient energy sources for consumer electronics, a comprehensive power management system is necessary. 46,47 To meet the DC power supply requirement of most electronic devices, the alternating current electric output from piezoelectric material is first converted to DC signal by using a rectifying bridge. 48,49 Then, a DC-DC buck converter is often used for impedance adaption and voltage regulation. 50 In this work, the comprehensive energy harvesting system uses an energy harvesting module based on a nanopower energy harvesting power supply (LTC3588-1, Linear Technology Corp.) to harvest the mechanical energy, as shown in Figure 4a. The FENG generates random electric pulses that are managed by LTC3588-1 as the first stage, which produces a DC output. As long as the continuous mechanical energy source is present, the harvested and regulated energy can be used to power electronic devices or to charge a rechargeable battery (CBC012, a cutoff voltage of 3 V) for energy storage (Figure S9, Supporting Information). Here, we present a method for powering an electronic device, while charging a backup battery by implementing an integrated power management chip (CBC3112) as a second stage. CBC3112 is able to supply a constant DC voltage, typically of 3.3 V, which can be connected to the electronic device to be powered. Meanwhile, it sends any excessive energy to an internal secondary battery (a cutoff voltage of 2.75 V) for energy storage. As shown in Figure 4a,  $V_{\rm DD}$  is internally applied to a charge pump  $V_{\rm CHG}$ , which contains a flying capacitor  $C_{FLY}$  in its voltage doubler circuit for charging the internal integrated backup battery  $V_{\rm BAT}$ .

When EN terminal asserts high (i.e., when CBC3112 senses a voltage generated by the device), the charge pump is activated and  $V_{\rm BAT}$  is being charged by  $V_{\rm DD}$ . The output voltage  $V_{\rm OUT}$  can either be supplied from  $V_{\rm DD}$  or  $V_{\rm BAT}$  depending on the switchover voltage threshold determined by  $V_{\rm MODE}$ .

Figure 4b shows unregulated direct charging profiles for capacitors with different capacitances, where the voltage across the capacitor continuously increases with the charging operation. The voltage output regulation realized by LTC3588-1 is shown in Figure 4c, where the output voltage is regulated at a constant voltage of 3.6 V. After the system enters the regulation mode, the excessive energy is stored in C<sub>STORAGE</sub> with the increasing voltage measured across the capacitor. By further comparing the voltage drop at  $C_{STORAGE}$ and increase in C<sub>OUT</sub>, the energy transfer efficiency of this energy harvesting module is estimated to be 38.5%. The output DC power can be directly used for powering electronic devices (load) or charging a battery (energy storage). Figure 4d shows the charging profile of a rechargeable solid state chip battery CBC012. The battery is being charged at a constant voltage of 3.6 V and is partially charged after 15 min of a mechanical force of an amplitude 78 N and frequency 4.26 Hz applied to the device. The discharging profile is presented in Figure 4e to demonstrate the energy stored in the battery. When a second stage power management chip CBC3112 is connected to the output terminal of LTC3588-1, the combined system is able to simultaneously output a constant DC power and transfer the excessive energy from  $C_{STORAGE}$  to an embedded integrated battery. Figure 4f shows the input and output voltages of CBC3112 as a second stage. Since CBC3112 sends part of the energy to the internal battery as energy storage, fluctuations are observed in the voltage, which are not observed when charging battery chip CBC012, as shown in Figure 4d. Figure 4g shows the discharging profile of the internal battery. More details on the operation of the energy harvesting module are found in the Supporting Information.

By utilizing ambient mechanical energy, electronic devices can be powered solely by the energy harvesting modules like to the ones described earlier. Figure 5a shows the demonstration of powering a commercial 3 V LCD screen by combining an eight-layer FENG device with a two-stage energy harvesting system (see Supporting Information Movie S1). This system is capable of delivering a constant DC power, while storing the excessive energy to an integrated chip battery. During the normal operation, the word "FENG" is displayed on the screen, while storing the energy shown in Figure 4g. Figure 5b shows the implementation of the energy harvesting system (one stage) for the application of charging a rechargeable solid state battery (see Supporting Information Movie S2). The charged battery is used to power three LED lights. Figure 5c,d demonstrates utilizing harvested energy to power commercial 1.8 V humidity sensor and temperature sensor, respectively (see Supporting Information Movies S3 and S4). The same LCD screen, which is shown in Figure 5a, can also be selfpowered by this one-stage energy harvesting module, as shown in Figure 5e (see Supporting Information Movie S5).

#### 3. CONCLUSIONS

In summary, the present work shows a comprehensive approach that describes the use of PPFE films as nanogenerators and their integration into systems that can convert mechanical energy to electrical energy for either energy storage or powering of electronic devices. The generated electric output and its dynamic behavior is characterized in terms of open circuit voltage, short circuit current, transferred charge, efficiency of the complete system, and delivered power. The output current and voltage are found to be related to the input mechanical loads and velocities. Various resistive loads have been used to find the maximum power output, which is around 0.902  $\mu W$  under a linear  $F_1$  with 600  $M\Omega$ . Therefore, the energy conversion efficiency is calculated to be 0.14% for the performed experiment. To effectively harvest the energy from ambient mechanical sources, a comprehensive energy harvesting module with a corresponding power management circuitry has been proposed, which can be used for powering electronic devices, charging a solid state battery chip, or both.

#### 4. EXPERIMENTAL SECTION

4.1. Device Fabrication. The fabrication process starts with a PP film filled with inorganic silicates as a stress raiser. When the film is experiencing a biaxial in-plane tensile stress, microcrack occurs when the stress level is higher than the material's cohesive strength and propagates in the two perpendicular direction. Then, high nitrogen gas (~5 MPa) is introduced to allow the diffusion of gas into the material. Next, the high-pressure atmosphere is suddenly removed, which results a quick swelling of the cracks and forms ellipsoid voids. A heat siting process at ~100 °C is followed to stabilize the void structure strength. After that high electric field is applied to induce plasma discharging inside the voids, charges with opposite polarities, therefore, accumulate on two surfaces of the void and form the permanent giant dipoles. The electrodes metalization is achieved by sputter coating of silver thin films on both sides of the PPFE film. Conductive copper tape is used to attach the copper wires to silver electrodes for output connection. Finally, the device is encapsulated in between two protective polyimide layers.

**4.2. Measurement of Electric Output.** The voltage and current output are both measured by the Keithley 2450 Source Meter. The battery charging and discharging profiles are measured by the Keithley 2182 Nanovoltmeter. The mechanical force input is first measured in

terms of the voltage allocated to the varistor-based force sensor A502. The force sensor calibration is illustrated in Supporting Information.

#### ASSOCIATED CONTENT

# Supporting Information

The Supporting Information is available free of charge on the ACS Publications website at DOI: 10.1021/acsami.9b02233.

Force sensor calibration; fabrication process of PPFE film; sputtering coating system; piezoelectric effect of FENG; multilayer structure device; operation of energy harvesting module; energy conversion efficiency (PDF)

Energy harvesting is demonstrated by powering a commercial available 3VLCD screen through a two-stage system (Movie S1); energy harvesting is demonstrated by charging a rechargeable chip battery-through a one-stage system (Movie S2) (ZIP)

Energy harvesting is demonstrated by powering a commercial humiditysensor through a one-stage system (Movie S3); energy harvesting is demonstrated by powering a commercial temperaturesensor through a one-stage system (Movie S4) (ZIP)

Energy harvesting is demonstrated by powering a commercial LCD screenthrough a one-stage system (Movie S5) (ZIP)

## AUTHOR INFORMATION

## **Corresponding Author**

\*E-mail: nelsons@egr.msu.edu.

#### ORCID

Nelson Sepúlveda: 0000-0002-9676-8529

#### Note:

The authors declare no competing financial interest.

## ACKNOWLEDGMENTS

This work was supported by the National Science Foundation (NSF ECCS Award: ECCS-1744273). The authors also would like to thank the Composite Materials and Structures Center (CMSC) at Michigan State University.

#### REFERENCES

- (1) Mu, E.; Wu, Z.; Wu, Z.; Chen, X.; Liu, Y.; Fu, X.; Hu, Z. A Novel Self-powering Ultrathin TEG Device based on Micro/Nano Emitter for Radiative Cooling. *Nano Energy* **2019**, *55*, 494–500.
- (2) Sun, S.; Ning, D.; Yang, J.; Du, H.; Zhang, S.; Li, W.; Nakano, M. Development of an MR Seat Suspension with Self-powered Generation Capability. *Smart Mater. Struct.* **2017**, *26*, No. 085025.
- (3) Chen, X.; Parida, K.; Wang, J.; Xiong, J.; Lin, M.-F.; Shao, J.; Lee, P. S. A Stretchable and Transparent Nanocomposite Nanogenerator for Self-powered Physiological Monitoring. ACS Appl. Mater. Interfaces 2017, 9, 42200–42209.
- (4) Shen, C.; Xu, S.; Xie, Y.; Sanghadasa, M.; Wang, X.; Lin, L. A Review of On-chip Micro Supercapacitors for Integrated Self-powering Systems. *J. Microelectromech. Syst.* **2017**, *26*, 949–965.
- (5) Talite, M. J.; Huang, H.-Y.; Wu, Y.-H.; Sena, P. G.; Cai, K.-B.; Lin, T.-N.; Shen, J.-L.; Chou, W.-C.; Yuan, C.-T. Greener Luminescent Solar Concentrators with High Loading Contents Based on in Situ Cross-Linked Carbon Nanodots for Enhancing Solar Energy Harvesting and Resisting Concentration-Induced Quenching. ACS Appl. Mater. Interfaces 2018, 10, 34184–34192.
- (6) Li, R.; Xiang, X.; Tong, X.; Zou, J.; Li, Q. Wearable Double-Twisted Fibrous Perovskite Solar Cell. *Adv. Mater.* **2015**, 27, 3831–3835

- (7) Thielen, M.; Sigrist, L.; Magno, M.; Hierold, C.; Benini, L. Human Body Heat for Powering Wearable Devices: From Thermal Energy to Application. *Energy Convers. Manage.* **2017**, *131*, 44–54.
- (8) Kotipalli, V.; Gong, Z.; Pathak, P.; Zhang, T.; He, Y.; Yadav, S.; Que, L. Light and Thermal Energy Cell Based on Carbon Nanotube Films. *Appl. Phys. Lett.* **2010**, *97*, No. 124102.
- (9) Beeby, S. P.; Tudor, M. J.; White, N. Energy Harvesting Vibration Sources for Microsystems Applications. *Meas. Sci. Technol.* **2006**, *17*, No. R175.
- (10) Turkmen, A. C.; Celik, C. Energy harvesting with the Piezoelectric Material Integrated Shoe. *Energy* **2018**, *150*, 556–564.
- (11) Lagomarsini, C.; Jean-Mistral, C.; Lombardi, G.; Sylvestre, A. Hybrid Piezoelectric-electrostatic Generators for Wearable Energy Harvesting Applications. *Smart Mater. Struct.* **2019**, 28, No. 035003.
- (12) Huan, Y.; Zhang, X.; Song, J.; Zhao, Y.; Wei, T.; Zhang, G.; Wang, X. High-performance Piezoelectric Composite Nanogenerator based on Ag/(K, Na) NbO3 Heterostructure. *Nano Energy* **2018**, *S0*, 62–69.
- (13) Parangusan, H.; Ponnamma, D.; Al-Maadeed, M. A. A. Stretchable Electrospun PVDF-HFP/Co-ZnO Nanofibers as Piezo-electric Nanogenerators. *Sci. Rep.* **2018**, *8*, No. 754.
- (14) Zhang, X.-S.; Han, M.-D.; Wang, R.-X.; Zhu, F.-Y.; Li, Z.-H.; Wang, W.; Zhang, H.-X. Frequency-Multiplication High-Output Triboelectric Nanogenerator for Sustainably Powering Biomedical Microsystems. *Nano Lett.* **2013**, *13*, 1168–1172.
- (15) Chun, J.; Kim, J. W.; Jung, W.-s.; Kang, C.-Y.; Kim, S.-W.; Wang, Z. L.; Baik, J. M. Mesoporous Pores Impregnated with Au Nanoparticles as Effective Dielectrics for Enhancing Triboelectric Nanogenerator Performance in Harsh Environments. *Energy Environ. Sci.* 2015, 8, 3006–3012.
- (16) Zhang, R.; Hummelgård, M.; Örtegren, J.; Olsen, M.; Andersson, H.; Yang, Y.; Olin, H. Human Body Constituted Triboelectric Nanogenerators as Energy Harvesters, Code Transmitters, and Motion Sensors. ACS Appl. Energy Mater. 2018, 1, 2955—2960.
- (17) Zhao, X.; Kang, Z.; Liao, Q.; Zhang, Z.; Ma, M.; Zhang, Q.; Zhang, Y. Ultralight, Self-powered and Self-adaptive Motion Sensor based on Triboelectric Nanogenerator for Perceptual Layer Application in Internet of Things. *Nano Energy* **2018**, *48*, 312–319.
- (18) Li, W.; Torres, D.; Díaz, R.; Wang, Z.; Wu, C.; Wang, C.; Wang, Z. L.; Sepúlveda, N. Nanogenerator-based Dual-functional and Self-powered Thin Patch Loudspeaker or Microphone for Flexible Electronics. *Nat. Commun.* **2017**, *8*, No. 15310.
- (19) Zhang, Y.; Bowen, C. R.; Ghosh, S. K.; Mandal, D.; Khanbareh, H.; Arafa, M.; Wan, C. Ferroelectret Materials and Devices for Energy Harvesting Applications. *Nano Energy* **2019**, *57*, 118–140.
- (20) Ghosh, S. K.; Xie, M.; Bowen, C. R.; Davies, P. R.; Morgan, D. J.; Mandal, D. A Hybrid Strain and Thermal Energy Harvester based on an Infra-red Sensitive Er 3+ Modified Poly (vinylidene fluoride) Ferroelectret Structure. Sci. Rep. 2017, 7, No. 16703.
- (21) Wang, Z. L. On Maxwell's Displacement Current for Energy and Sensors: The Origin of Nanogenerators. *Mater. Today* **2017**, *20*, 74–82.
- (22) Zhu, G.; Lin, Z.-H.; Jing, Q.; Bai, P.; Pan, C.; Yang, Y.; Zhou, Y.; Wang, Z. L. Toward Large-scale Energy Harvesting by a Nanoparticle-enhanced Triboelectric Nanogenerator. *Nano Lett.* **2013**, *13*, 847–853.
- (23) Ghosh, S. K.; Sinha, T. K.; Mahanty, B.; Mandal, D. Self-poled Efficient Flexible "Ferroelectretic" Nanogenerator: A New Class of Piezoelectric Energy Harvester. *Energy Technol.* **2015**, *3*, 1190–1197.
- (24) Wang, B.; Liu, C.; Xiao, Y.; Zhong, J.; Li, W.; Cheng, Y.; Hu, B.; Huang, L.; Zhou, J. Ultrasensitive Cellular Fluorocarbon Piezoelectret Pressure Sensor for Self-powered Human Physiological Monitoring. *Nano Energy* **2017**, 32, 42–49.
- (25) Rupitsch, S. J.; Lerch, R.; Strobel, J.; Streicher, A. Ultrasound Transducers Based on Ferroelectret Materials. *IEEE Trans. Dielectr. Electr. Insul.* **2011**, *18*, 69–80.

- (26) Lindner, M.; Hoislbauer, H.; Schwodiauer, R.; Bauer-Gogonea, S.; Bauer, S. Charged Cellular Polymers with "Ferroelectretic" Behavior. *IEEE Trans. Dielectr. Electr. Insul.* **2004**, *11*, 255–263.
- (27) Hamdi, O.; Mighri, F.; Rodrigue, D. Time and Thermal Stability Improvement of Polyethylene Ferroelectrets. *J. Appl. Polym. Sci.* **2019**, No. 47646.
- (28) Bauer, S. Piezo-, Pyro-and Ferroelectrets: Soft Transducer Materials for Electromechanical Energy Conversion. *IEEE Trans. Dielectr. Electr. Insul.* **2006**, 13, 953–962.
- (29) Li, W.; Torres, D.; Wang, T.; Wang, C.; Sepúlveda, N. Flexible and Biocompatible Polypropylene Ferroelectret Nanogenerator (FENG): on the Path Toward Wearable Devices Powered by Human Motion. *Nano Energy* **2016**, *30*, 649–657.
- (30) Luo, Z.; Zhu, D.; Shi, J.; Beeby, S.; Zhang, C.; Proynov, P.; Stark, B. Energy Harvesting Study on Single and Multilayer Ferroelectret Foams under Compressive Force. *IEEE Trans. Dielectr. Electr. Insul.* **2015**, 22, 1360–1368.
- (31) Cao, Y.; Li, W.; Figueroa, J.; Wang, T.; Torres, D.; Wang, C.; Wang, Z. L.; Sepulveda, N. Impact-activated Programming of Electro-Mechanical Resonators Through Ferroelectret Nanogenerator (FENG) and Vanadium Dioxide. *Nano Energy* **2018**, *43*, 278–284.
- (32) Junnila, S.; Akhbardeh, A.; Varri, A.; Koivistoinen, T. In An EMFi-film Sensor Based Ballistocardiographic Chair: Performance and Cycle Extraction Method. Signal Processing Systems Design and Implementation; IEEE Workshop, 2005; pp 373–377.
- (33) Fan, F.-R.; Tian, Z.-Q.; Wang, Z. L. Flexible Triboelectric Generator. *Nano Energy* **2012**, *1*, 328–334.
- (34) Xu, Z.; et al. Boosting the Efficient Energy Output of Electret Nanogenerators by Suppressing Air Breakdown under Ambient Conditions. ACS Appl. Mater. Interfaces 2019, 11, 3984–3989.
- (35) Si, S. K.; Karan, S. K.; Paria, S.; Maitra, A.; Das, A. K.; Bera, R.; Bera, A.; Halder, L.; Khatua, B. B. A Strategy to Develop an Efficient Piezoelectric Nanogenerator Through ZTO Assisted γ-phase Nucleation of PVDF in ZTO/PVDF Nanocomposite for Harvesting Bio-mechanical Energy and Energy Storage Application. *Mater. Chem. Phys.* **2018**, 213, 525–537.
- (36) Xi, Y.; Wang, J.; Zi, Y.; Li, X.; Han, C.; Cao, X.; Hu, C.; Wang, Z. High Efficient Harvesting of Underwater Ultrasonic Wave Energy by Triboelectric Nanogenerator. *Nano Energy* **2017**, 38, 101–108.
- (37) Wang, X.; Niu, S.; Yin, Y.; Yi, F.; You, Z.; Wang, Z. L. Triboelectric Nanogenerator Based on Fully Enclosed Rolling Spherical Structure for Harvesting Low-Frequency Water Wave Energy. Adv. Energy Mater. 2015, 5, No. 1501467.
- (38) Zhang, X.; Pondrom, P.; Sessler, G. M.; Ma, X. Ferroelectret Nanogenerator with Large Transverse Piezoelectric Activity. *Nano Energy* **2018**, *50*, 52–61.
- (39) Su, Y.; Dagdeviren, C.; Li, R. Measured Output Voltages of Piezoelectric Devices depend on the Resistance of Voltmeter. *Adv. Funct. Mater.* **2015**, 25, 5320–5325.
- (40) Xie, L.; Cai, M. Increased Piezoelectric Energy Harvesting from Human Footstep Motion by Using an Amplification Mechanism. *Appl. Phys. Lett.* **2014**, *105*, No. 143901.
- (41) Wu, N.; Wang, Q.; Xie, X. Ocean Wave Energy Harvesting with a Piezoelectric Coupled Buoy Structure. *Appl. Ocean Res.* **2015**, *50*, 110–118.
- (42) Zhang, J.; Fang, Z.; Shu, C.; Zhang, J.; Zhang, Q.; Li, C. A Rotational Piezoelectric Energy Harvester for Efficient Wind Energy Harvesting. Sens. Actuators, A 2017, 262, 123–129.
- (43) Chen, T.; Xia, Y.; Liu, W.; Liu, H.; Sun, L.; Lee, C. A Hybrid Flapping-blade Wind Energy Harvester Based on Vortex Shedding Effect. J. Microelectromech. Syst. 2016, 25, 845–847.
- (44) Kärki, S.; Lekkala, J. A Lumped-Parameter Transducer Model for Piezoelectric and Ferroelectret Polymers. *Measurement* **2012**, *45*, 453–458.
- (45) Wang, S.; Lin, Z.-H.; Niu, S.; Lin, L.; Xie, Y.; Pradel, K. C.; Wang, Z. L. Motion Charged Battery as Sustainable Flexible-Power-Unit. ACS Nano 2013, 7, 11263–11271.
- (46) Niu, S.; Wang, X.; Yi, F.; Zhou, Y. S.; Wang, Z. L. A universal Self-Charging System Driven by Random Biomechanical Energy for

ī

Sustainable Operation of Mobile Electronics. *Nat. Commun.* **2015**, *6*, No. 8975.

- (47) Wu, L.; Do, X.-D.; Lee, S.-G.; Ha, D. S. A Self-Powered and Optimal SSHI Circuit Integrated with an Active Rectifier for Piezoelectric Energy Harvesting. In *IEEE Transactions on Circuits and Systems I: Regular Papers*; IEEE, 2017; pp 537–549.
- (48) Guyomar, D.; Badel, A.; Lefeuvre, E.; Richard, C. Toward Energy Harvesting Using Active Materials and Conversion Improvement by Nonlinear Processing. In *IEEE Transactions on Ultrasonics, Ferroelectrics, and Frequency Contro*; IEEE, 2005; pp 584–595.
- (49) Ottman, G. K.; Hofmann, H. F.; Lesieutre, G. A. Optimized Piezoelectric Energy Harvesting Circuit Using Step-down Converter in Discontinuous Conduction Mode. In *IEEE Transactions on Power Electronics*; IEEE, 2003; pp 696–703.
- (50) Kim, H.; Priya, S.; Stephanou, H.; Uchino, K. Consideration of Impedance Matching Techniques for Efficient Piezoelectric Energy Harvesting. In *IEEE transactions on Ultrasonics, Ferroelectrics, and Frequency Control*; IEEE, 2007; pp 1851–1859.